5-30-2020

Constraining an Ocean Model Under Getz Ice Shelf, Antarctica, Using A Gravity-Derived Bathymetry

Romain Millan

Pierre St-Laurent
Virginia Institute of Marine Science

Eric Rignot

et al

Geophysical Research Letters

Key Points:
- Sub-ice shelf bathymetry reconstructed with a 3D inversion of gravity data reveals one of the deepest ice shelf cavities in West Antarctica
- An ocean model coupled with the new bathymetry indicates pathways where warm ocean water enters the cavity
- The new bathymetry helps elucidate the recent evolution of Getz glaciers and explain why Getz is a large producer of meltwater

Supporting Information:
- Supporting Information S1
- Movie S1

Correspondence to:
R. Millan,
romain.millan@univ-grenoble-alpes.fr

Constraining an Ocean Model Under Getz Ice Shelf, Antarctica, Using A Gravity-Derived Bathymetry

Romain Millan[1,2] iD, **Pierre St-Laurent**[3,4] iD, **Eric Rignot**[2,5,6] iD, **Mathieu Morlighem**[2] iD, **Jeremie Mouginot**[1,2] iD, and **Bernd Scheuchl**[2] iD

[1]IGE, Univ. Grenoble Alpes, CNRS, IRD, Grenoble INP, Grenoble, France, [2]Department of Earth System Science, University of California Irvine, Irvine, CA, USA, [3]Center for Coastal Physical Oceanography, Old Dominion University, Norfolk, VA, USA, [4]Virginia Institute of Marine Science, William & Mary, Gloucester Point, VA, USA, [5]Jet Propulsion Laboratory, Caltech, Pasadena, CA, USA, [6]Department of Civil and Environmental Engineering, University of California Irvine, Irvine, CA, USA

Abstract Getz Ice Shelf, the largest producer of ice shelf meltwater in Antarctica, buttresses glaciers that hold enough ice to raise sea level by 22 cm. We present a new bathymetry of its sub-ice shelf cavity using a three-dimensional inversion of airborne gravity data constrained by multibeam bathymetry at sea and a reconstruction of the bedrock from mass conservation on land. The new bathymetry is deeper than previously estimated with differences exceeding 500 m in a number of regions. When incorporated into an ocean model, it yields a better description of the spatial distribution of ice shelf melt, specifically along glacier grounding lines. While the melt intensity is overestimated because of a positive bias in ocean thermal forcing, the study reveals the main pathways along which warm oceanic water enters the cavity and corroborates the observed rapid retreat of Berry Glacier along a deep channel with a retrograde bed slope.

Plain Language Summary The Getz Ice Shelf is a major ice shelf in West Antarctica that is rapidly melting. Its exposure to warm oceanic water has made it the largest producer of ice shelf meltwater in Antarctica. To understand its evolution and the impact on sea level rise of the glaciers that flow into it, it is essential to obtain a better description of the bathymetry beneath its hundreds of meters of floating ice. We use a combination of airborne gravity and other data to infer the depth of the cavity. We find the seabed to be in several regions more than 500 m deeper than previously reported, hence revealing one of the deepest ice shelf cavities in West Antarctica. When used in combination with an ocean model, the bathymetry helps to better explain the spatial variability in melt observed from remote sensing data, the pathways for warm waters to reach the ice shelf, and the recent evolution of selected glaciers.

1. Introduction

The West Antarctic Ice Sheet (WAIS) is a major contributor to sea level rise, accounting for 7.3 mm of sea level rise between 1979 and 2017 (Rignot et al., 2019). Mass loss from the glaciers flowing into the Amundsen Sea Embayment has been attributed to the enhanced intrusion of warm oceanic water, which melts ice near the grounding line, reduces basal resistance to flow, and increases ice discharge into the ocean (Rignot et al., 2019). The role of ice shelves in buttressing the glaciers has been well documented and modeled (Dupont & Alley, 2005; Gudmundsson et al., 2019; Pritchard et al., 2012). Ice shelf mass balance is controlled by the rate of calving and basal melt, the latter of which depends on the advection of ocean heat into the sub-ice shelf cavity (Jourdain et al., 2017).

The intrusion of warm water into cavities is controlled by the seabed topography (Nitsche et al., 2007), which must be estimated beneath hundreds of meters of floating ice. The thickness of the floating ice also influences basal melt rates via the pressure dependence of the freezing temperature of seawater (Fujino et al., 1974), which increases the melting potential of water masses beneath deep ice shelf drafts.

Getz Ice Shelf (GIS) is located west of the Amundsen Sea Embayment with an east-west major axis (Figure 1a). It buttresses an ice volume equivalent to a sea level rise of 22 cm (Morlighem et al., 2020; Rignot et al., 2019). Along with George VI and Abbot, GIS is one of the largest ice shelves in WAIS (33,367 km^2) (Rignot et al., 2013) (Figure 1a) and is also the largest producer of ice shelf meltwater in Antarctica, contributing 144.9 ± 14 Gt/yr of freshwater, equivalent to an area-average melt rate of
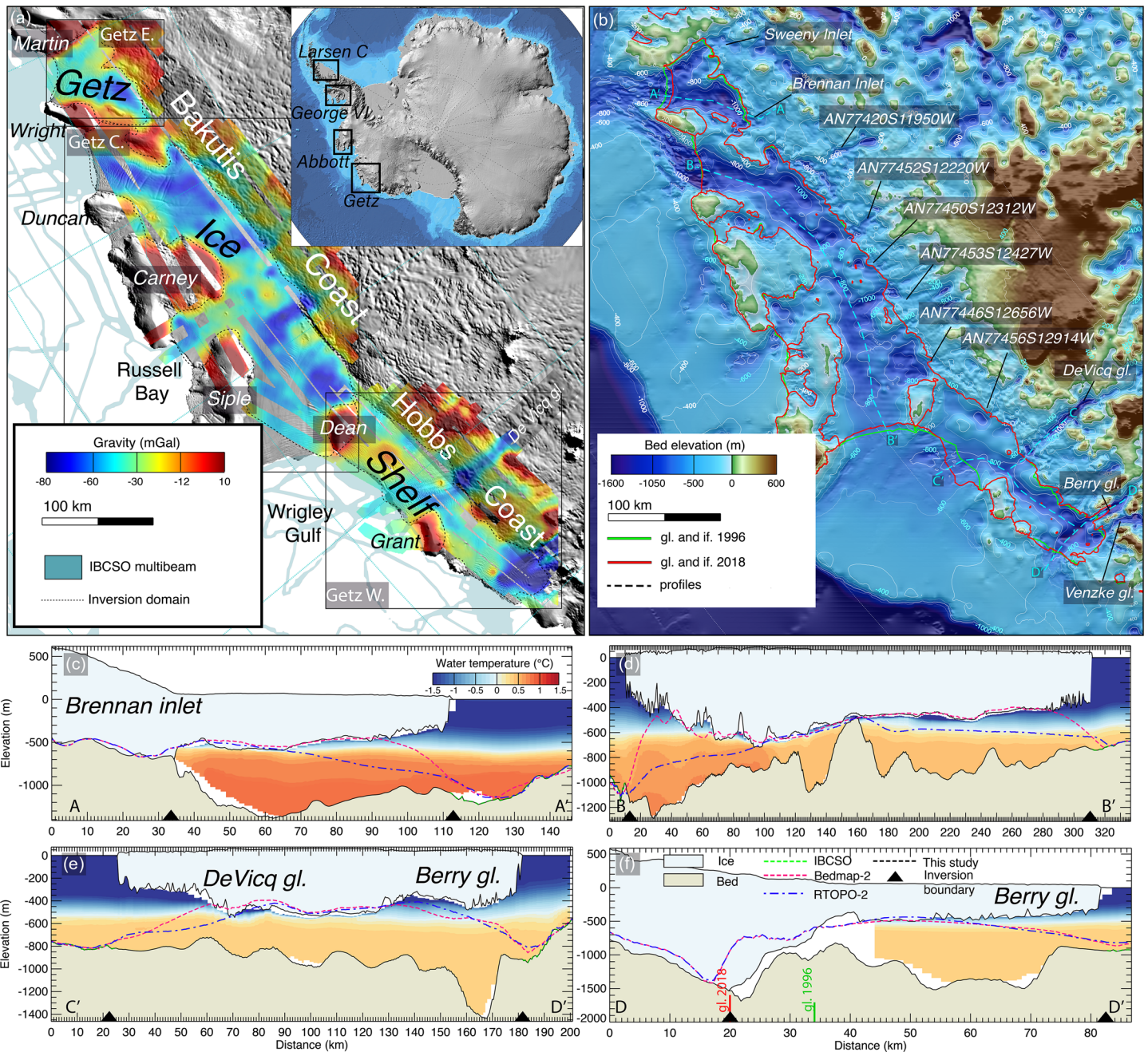
Figure 1. (a) Free-air gravity anomaly over the Getz Ice Shelf, West Antarctica with subregions Getz East (Getz E.), Central (Getz C.), and West (Getz W.) overlaid on a MODIS mosaic of Antarctica. Multibeam echo sounding data from IBCSO.1 are light grey. The limits of the gravity inversion are thin black dashed lines. Inset map shows the position of Getz Ice Shelf in Antarctica along with the location of other major ice shelves of the region and mentioned in this study. (b) Bathymetry derived from the 3D inversion color coded from brown/yellow and green (above sea level) to light blue and dark blue (<−1,500 m), with thin contours every 100 m and thick contours every 400 m. Glacier grounding lines and ice fronts are shown for year 1996 (green) and for year 2018 (red). (f) Profiles are shown as dashed blue lines. (c–f) Surface elevation along A-A', B-B', C-D', and D-D' with bed elevation from this study (black), Bedmap2 (purple dashed line), RTopo-2 (blue dashed line), and multibeam echo sounding (green dashed line). Ice is light blue, seabed is light brown, and the ocean is shaded with the water temperature from the 3D ocean model (average of years 2006–2008).

4.3 ± 0.4 m/yr. The ice shelf thinned by 2 ± 0.3 m/yr between 2003 and 2008, equivalent to a mass loss of 67.6 ± 12 Gt/yr, or 50% of the combined mass input from accumulation of snowfall on the ice shelf surface and from the inflow of land ice at the grounding line. A recent study indicates that the drainage basin of Getz has lost 363 Gt of mass since 1979, or 1-mm sea level rise equivalent (Rignot et al., 2019).

Hydrographic surveys in the region of the GIS (Jacobs et al., 2013) have revealed the presence of warm Circumpolar Deep Water (CDW) at the shelf break and modified CDW (mCDW) in front of the ice shelf. Following Jacobs et al. (2013), CDW is defined by temperature ≥1°C and salinity ≥34.6 psu, while mCDW is described with temperature <1°C and salinity in the range 34.5–34.6 psu. Furthermore, mCDW represents a segment of the mixing line between CDW and cold "Winter Water" (Jacobs et al., 2013, their Figure 4c), the latter dominating the upper ~300 m of the water column on the continental shelf of the western Amundsen Sea (e.g., Sherrell et al., 2015). The presence of mCDW in front of Getz indicates that CDW is transported over the continental shelf and becomes gradually diluted ("modified") as it progresses toward the Getz cavity. However, the pathways used by this CDW/mCDW to reach the grounding line of Getz remain poorly known (Assmann et al., 2019). In order to project the evolution of this dynamic sector, it is critical to understand these pathways and reproduce the pattern and intensity of ice shelf melt using an ocean model. Indeed, the strongest limitation of predictive models is the poor representation of the shape of the seafloor under the ice shelf, which has a major impact on the ocean circulation in the cavity.

Currently available bathymetry beneath the GIS is the result of a mathematical interpolation between the front of the ice shelf and the grounding line. This approach forces the ice shelf to have a shallow cavity, being grounded or close to it, which implies further arbitrary model adjustments (Arndt et al., 2013; Fretwell et al., 2013; Le Brocq et al., 2010; Timmermann et al., 2010). As a consequence, the large uncertainties related to these techniques impair our understanding of ice-ocean interactions (Dutrieux et al., 2014; Millan et al., 2017). Characterizing sub-ice shelf cavities with in situ data, for example, seismic profiles or from robotic devices (Muto et al., 2013), is possible but prohibitively expensive and logistically challenging over such a vast surface area. When properly constrained at the boundary of the inversion domain and in as many locations as possible, airborne gravity is an efficient remote sensing technique for reconstructing bathymetry over large areas (An et al., 2019; Hodgson et al., 2019; Millan et al., 2017; Tinto & Bell, 2011; Tinto et al., 2019). Relevant and reliable boundary conditions include reconstructions of bed topography beneath grounded ice using a mass conservation method (Morlighem et al., 2020) and multibeam echo sounding (MBES) data offshore from international ship surveys (Arndt et al., 2013). These constraints significantly reduce the uncertainty in the solution of the inversion and offer a smooth transition from the seabed to the bed beneath grounded ice. Having a smooth transition at the grounding line is indeed crucial to avoid large discontinuities which create artifacts in ice sheet and ocean numerical models.

We present a three-dimensional (3D) inversion of the bathymetry of GIS derived from airborne gravity data constrained by MBES data from the International Bathymetric Chart of the Southern Ocean (IBCSO) offshore and BedMachine Antarctica inland (Morlighem et al., 2020). We then use our inferred bathymetry in an ocean numerical model to reveal the pathways of warm water into the sub-ice shelf cavity, calculate ice shelf melt rates from the model, and compare the results with those obtained using prior RTopo-2 bathymetry (Schaffer et al., 2016) and remote sensing observations. We discuss the impact of the new bathymetry in interpreting ice-ocean interactions and glacier retreat in this major sector of WAIS.

2. Data and Methods

2.1. OIB Gravity Data and Inversion

We use airborne gravity data acquired by NASA's Operation IceBridge (OIB) mission between October 2009 and November 2014 using the Sander Geophysics Airborne Inertially Referenced gravimeter (AIRGrav system) (Figure 1a). Data were acquired with a ground clearance of 400 m, at a flight speed of 140–150 m/s, with a sampling frequency of 128 Hz. Free air gravity anomalies were generated with Eötvös, normal gravity, free-air, static, and level corrections. The gravity anomalies were filtered with a 70-s full-wavelength filter, resulting in an average spatial resolution of 4.9 km. We exclude data collected above 1,500-m elevation above the ice surface. Flight elevations are consistent (within 200 m) from one track to the next as the surveys were completed at a nominal elevation of 450 m above the ice surface. Hence, we do not upward continue the data (Hodgson et al., 2019). We divide the inversion domain into three subregions: (1) Getz East (Getz E.); (2) Getz Central (Getz C.), along Bakutis Coast, spanning from Wrigley Gulf on the west to Duncan Island in the east; and (3) Getz West (Getz W.), along Hobbs Coast, which includes DeVicq and Berry glaciers (Mouginot et al., 2019).

To perform the gravity inversion procedure, we use a semi-automatic processing chain developed using the Geosoft® Oasis Montaj software. For all subregions, we form an initial solution with three layers: (1) an ice layer (density $\rho = 0.917$ g/cm^3); (2) an ocean layer ($\rho = 1.028$ g/cm^3); and (3) a bedrock layer ($\rho = 2.67$ g/cm^3). At the edge of the domain, the inversion is constrained with a mass conservation reconstruction of the bedrock from BedMachine Antarctica inland (Morlighem et al., 2020) and IBCSO multibeam observations offshore (Arndt et al., 2013). The mass conservation method combines available radar ice thickness measurements with satellite surface flow velocity to determine the ice thickness between radar observations based on the principle of mass conservation (Morlighem et al., 2014). Within the domain, we identify pinning points where the ice shelf bottom touches the seabed using satellite radar interferometry (Rignot, 2001). The initial sub-ice shelf bathymetry uses the RTopo-2 map (Schaffer et al., 2016).

We calculate the difference between modeled and observed gravity where the bed is known and interpolate the results over a regular grid using a minimum curvature algorithm. In order to avoid short wavelength variations that cannot be captured by the gravimeter, we low-pass filter the results using a cutoff wavelength of 5 km. This grid provides an absolute reference for the data and accounts for large-scale spatial variations in the underlying geology (An et al., 2019; Hodgson et al., 2019). Spatial variations in density could indeed affect the solution, but these variations should be relatively well accounted for, when the inversion domain is surrounded by in situ observations. Hence, errors will increase over a large area when moving away from the constrained boundary, known grounding line depth, or available seismic data. Data gaps are replaced with the modeled gravity from the initial bathymetry solution as in An et al. (2019). Finally, we invert the bathymetry where it is currently not known and stop the optimization when the difference between modeled and measured gravity is below a user-provided arbitrary value of 0.1 mGal (An et al., 2019; Millan et al., 2017). We use the gravity misfit as a measure of the accuracy of the inversion, that is, the ability of the algorithm to properly fit the gravity anomalies.

2.2. Ocean Modeling

The new bathymetry is employed in a 3D ice shelf-sea ice-ocean model based on the Regional Ocean Modeling System (ROMS, Shchepetkin & McWilliams, 2005), which simulates the ocean circulation on the continental shelf of the Amundsen Sea and in the sub-ice shelf cavity. We use the model setup from St-Laurent et al. (2017) that has a uniform horizontal resolution of 1.5 km and 20 topography-following vertical levels. This version of the ocean model does not extend up to the 2018 grounding line of the glaciers feeding the GIS. Extending the domain to include this portion would require a complete revision of the model and its forcings. The ice shelf geometries, that is, areal extent, surface elevation, and draft elevation, are assumed to remain constant over the simulation period. The ice shelf and ocean are thermodynamically coupled with transfer coefficients that are functions of the model friction velocity (Dinniman et al., 2011; Holland & Jenkins, 1999).

We define three model experiments (referred to as Cases I, II, and III) to test the impact of the new bathymetry (Supporting Information, Figure S1). Case I is the optimal estimate combining the new bathymetry with the ice shelf draft from BedMachine Antarctica (Morlighem et al., 2020). Case II combines the new bathymetry and the ice shelf draft in RTopo-2 (Schaffer et al., 2016), which was also used in St-Laurent et al. (2017). Case III uses both the seabed and the ice shelf draft from RTopo-2 (Figure S1).

These topographic data sets must be modified to satisfy the numerical constraints of the ocean model. First, the bed topography is smoothed to minimize discontinuities (Haney, 1991; Shchepetkin & McWilliams, 2003). Areas where differences in elevation between the ice shelf draft and the seabed are less than 15 m are removed from the cavity domain. With these restrictions in place, the model covers 81% (Case III) to 96% (Case I) of the ice shelf area that is defined in BedMachine.

The salinity and temperature from a circumpolar model (Southern Ocean State Estimate, SOSE, Mazloff et al., 2010) are imposed at the open boundaries of the Amundsen model (see St-Laurent et al., 2017). SOSE is known to exhibit a warm bias on the continental shelf (Rodriguez et al., 2016), which affects both the thermocline depth and the temperature of the bottom layer at the western open boundary of the Amundsen model (137°W). In this study, this bias is partially mitigated by imposing an upper limit (2.5 K above freezing) on the water temperature at the western open boundary, based on in situ measurements

(Jacobs et al., 2013). This limit does not correct the thermocline depth; hence, a warm bias remains apparent in the western part of the model domain (see Section 3.2).

In the three experiments, the model is run over a 3-year period between 2011 and 2013, so that it adjusts to the bathymetry. The final state is used as the initial condition for a 3-year-long simulation (2006–2008) from which we extract time-averaged fields. The time period 2006–2008 is selected to coincide with Rignot et al. (2013) (years 2003–2008) and the 2007 hydrographic survey described in Jacobs et al. (2013). It is worth noting that the atmospheric product used to force the ocean model (Antarctic Mesoscale Prediction System; see St-Laurent et al., 2017) is not available prior to 2006, which explains the temporal mismatch between the spin-up and the simulation period. The same seasonal climatology of temperature and salinity is repeated at the lateral boundaries of the model throughout the duration of the simulation (see St-Laurent et al., 2017).

We examine the pathways of warm water by mapping the maximum water temperature within the layer satisfying the definitions of CDW (mostly present at the shelf break) or mCDW (continental shelf and ice shelf cavity). The temperature maximum represents the core of the layer and serves two purposes: (1) identify areas where mCDW is present and (2) illustrate the gradual dilution of warm water from the shelf break to the grounding line. A stream function, computed from the horizontal model velocity at the core of the CDW/mCDW layer, provides an indication of the horizontal circulation of this layer.

3. Results

3.1. New Bathymetric Model

The new bathymetry is on average 215 m deeper than Bedmap2, but differences greater than 500 m are observed in a number of regions such as the troughs leading to the Brennan Inlet, Duncan Island, Wrigley Gulf, and Berry Glacier (Figures 1c–1f). In previous estimates, none of the three subregions contained any major troughs (Figures 1c–1f). Differences with RTopo-2 exceed 500 m under Getz C. and E. and the western part of Getz W. near Berry Glacier (Figures S1 and 2f). After a comparison with other bathymetry products in other parts of WAIS, we conclude that the GIS has the deepest cavity over a region spanning from George VI to Ross Ice Shelf (Brisbourne et al., 2014; Cochran et al., 2014; Maslanyj, 1987; Millan et al., 2017; Tinto et al., 2019). The inversion error budget includes the error of the gravity measurements, which is 1.5 mGal based on crossover analysis, and the inversion misfit, which is 1.1 mGal. We find an uncertainty of ~45 m using a conversion factor of 5.8 mGal per 100 m (Millan et al., 2017). To further evaluate the quality of our results, we run another inversion over a subdomain with complete MBES coverage but only constrain the inversion over the periphery as in An et al. (2019). We find a difference with the MBES data of ~50 m, which is consistent with our prior calculation. Larger uncertainties are not excluded in areas where limited in situ observations are available to constrain the model (e.g., Getz C).

The cavity Getz E. has two main branches. The eastern branch is 1000 m deep, shallowing smoothly to 600 m at the grounding line of Sweeny Inlet (Figure 1b). The western branch is up to 1,450 m deep, with a sharp rise at the grounding line of Brennan Inlet, where the bed elevation rises from 1,200 to 650-m depth over 20 km (km 30 to km 50 in A-A′, Figure 1c). The Getz C region is divided into one smaller cavity, at the entrance of Russell Bay, and two main sub-cavities, one between Wright and Duncan islands to the east (which we refer to as the Wright-Duncan opening) and the other at the Siple-Dean opening, which is the entrance of Wrigley Gulf to the west. The two main cavities are separated by a 35-km ridge at - 600 m on its deepest section (Figure 1b). The eastern branch, which is the deepest, connects with glaciers AN77420S11950 W and AN77452S12220 W (names from United States Geological Survey convention); it deepens to <1,100 m along a 30 km wide trough that connects with the main eastern channel on the continental shelf that reaches Getz E. (Figure 1b). The Siple-Dean opening is broader, 800 m deep on average, and reaches the grounding lines of three major glaciers: AN77450S12312W, AN77453S12427 W, and AN77446S12656W. We have incomplete data coverage near the mouth of Wrigley Gulf, but the interpolated shoaling of the seafloor near the ice front is consistent with the gravity anomalies and smooth transitions with the MBES data.

Finally, Getz W. has two main channels. A shallow channel (500–800 m deep) at the Dean-Grant opening, on the east flank of Getz W., leads to AN77456S12914 W and DeVicq Glacier. A second deeper trough is located to the west of Grant Island (referred to as the Grant-West opening) and leads directly to Berry and Venzke glaciers. We note the presence of regular undulations in the inferred bed elevation (km 30–50 in
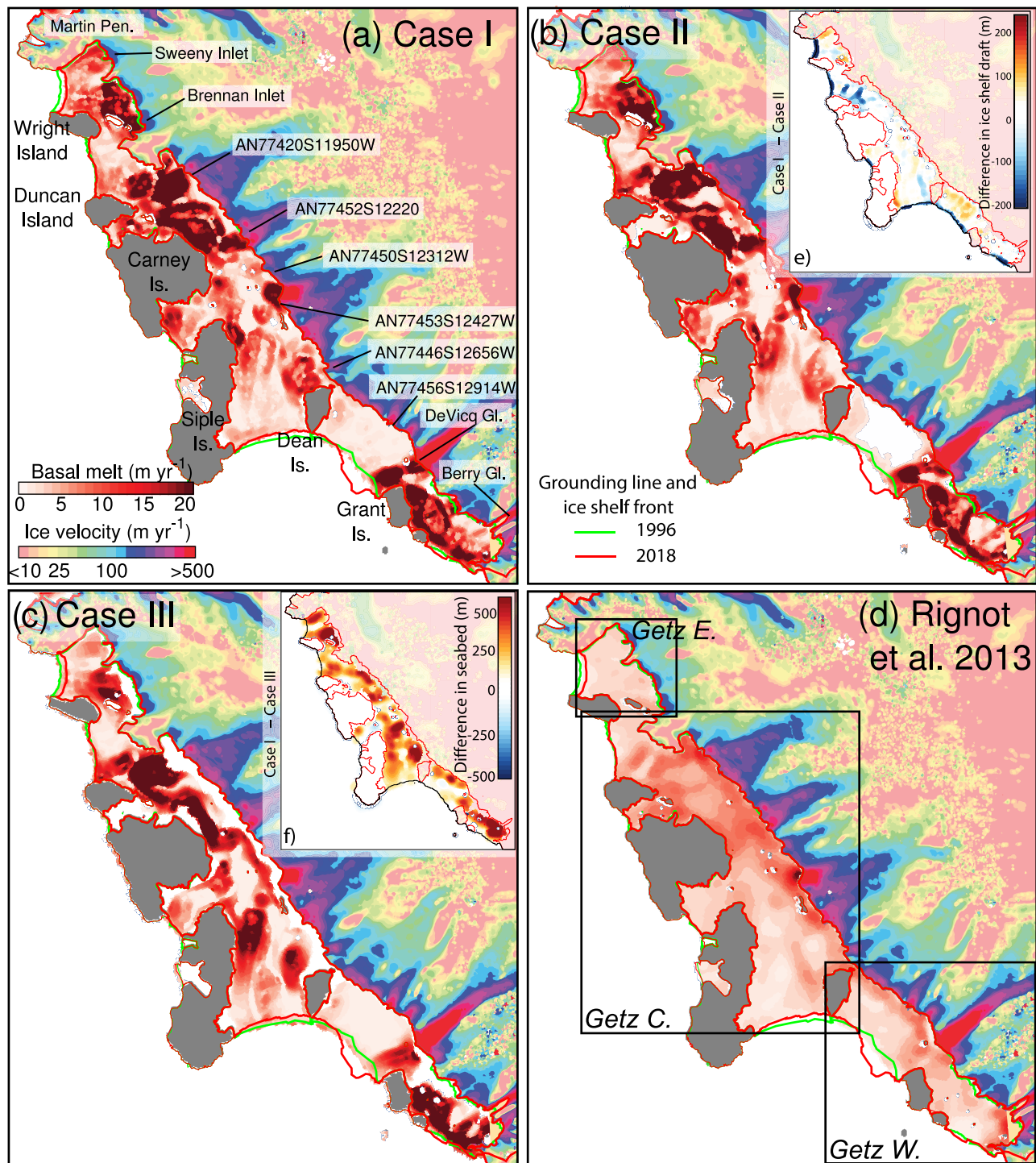
Figure 2. Basal melt rates calculated from the ocean model (average for the years 2006–2008) for Case I (a), II (b), and III (c). (d) Basal melt rates from remote sensing data for 2003–2008, estimated using a combination of radar sounder, ice velocity, and altimetry observations from Rignot et al. (2013). In (a–d), grounding line and ice front from 1996 are shown as a green solid line, while grounding line and ice front from 2018 are displayed as a red solid line. Ice velocity data on grounded ice are from Mouginot et al. (2019). Glacier names are from Rignot et al. (2019). Difference in ice shelf draft between Cases I and II is represented in inset (e), and difference in bathymetry between Cases III and I is represented in inset (f).

Figure 1f) which result from the minimum curvature interpolation scheme used to grid the gravity lines. Additional data would be required to better resolve the ice shelf cavity in this narrow trough. In BedMachine, the grounding line of Berry Glacier stands on a retrograde bed slope, which makes it prone to rapid retreat via marine ice sheet instability (Schoof, 2007). Indeed, a comparison of the 1996 versus 2018 grounding line indicates a 15-km retreat (Figure S2). During the processing, we revised the BedMachine solution with the 2018 grounding line, which revealed a recently formed, sub-ice shelf cavity in front of Berry Glacier along with a deep retrograde bed slope extending 40 km inland (Figures 1b and 1f).

3.2. Comparison of the Ocean Model Results with Hydrographic Surveys

We compare the ocean properties simulated by the 3D ocean model along the front of GIS with in situ observations from summer 2007 (Jacobs et al., 2013). These conditions will be referred to as the "thermal forcing" of the ice shelf. The three experiments capture the presence of warm water (e.g., >2 K above the in situ freezing temperature) at the ice shelf front, consistent with the 2007 survey (Figures S3–S6). Salinities of >34.5 psu are associated with either mCDW or CDW (see Section 1). East of Dean Island, Cases I–II reproduce the observed temperatures reasonably well, while Case III is ∼0.5 K too warm. West of Dean Island, the simulated thermocline in Cases I and II is too shallow by ∼100 m compared with the results of Jacobs et al. (2013) and too shallow by ∼200 m in Case III (see Section 2.2 for the bias origin). The model thus overestimates the temperature west of Dean Island in all cases, especially in Case III. For salinity, the model exhibits a positive bias of 0.1 psu in the eastern part of the ice shelf (all three cases), increasing to 0.2 psu in the western ice shelf (and 0.3 psu in Case III). The same biases (shallow thermocline and positive salinity bias) are apparent in an additional model-data comparison that uses the original casts of the 2007 cruise (Figure S7).

The surveys of 2000 and 2007 (Jacobs et al., 2013) revealed two locations where warm water consistently enters the ice shelf cavity: the Siple-Dean opening (see Assmann et al., 2019) and the Grant-West opening. These two inflows are strongly apparent in Cases I and II (dark blue shades, Figures S4e and S5e). Case III stands apart from the other cases, as the inflow across the Grant-West opening is accompanied by an outflow of similar magnitude (Figure S6e) because the channel between the continent and Grant Island is not resolved.

3.3. Basal Melt Rates

The ocean model produces high basal melt rates (≥20 m/yr) where the ice shelf draft is deep (Figures 2 and S1d) and thus likely to be in direct contact with warm water. These regions often coincide with deeper bathymetry (Figures 1 and S1), which presumably facilitates the access of warm and salty ocean water inside the cavity. Melt rates are the highest between Duncan and Carney Islands and around Grant Island (Figure 2). Areas of relatively shallow ice draft, such as the ice shelf front and around Dean Island, exhibit comparatively low melt rates (≤5 m/yr). In Case III (RTopo-2), the minimum water column thickness of 15 m is not satisfied in multiple parts of the cavity, especially near the grounding lines; hence, the model cannot simulate the melt rates in those areas (Figure 2c).

Total ice shelf melt varies from 217 (Case III) to 255 (Case II) and 267 Gt/yr (Case I), or 19% lower in Case III. Differences in cavity size, specifically along the grounding line, account for part of the difference since Case III resolves only 81% of the ice shelf area of BedMachine (26,604 km^2) versus 96% in Cases I and II (31,633 and 31,932 km^2, respectively). Furthermore, we note that the glacier area given in Rignot et al. (2013) is 34,018 km^2. Per unit area, basal melt is larger in Case III, which is consistent with its warmer temperatures (Figure S6). Over the exact same ice shelf extent (Case III area), the total ice shelf melt is 197, 187, and 205 Gt/yr for Cases I, II, and III, respectively. Compared with the remote sensing estimates of 145 Gt/yr, the modeled melt rates are therefore generally overestimated (Figure 2d).

4. Discussion

The inversion results are several hundreds of meters deeper than previous estimates, which could favor the intrusion of warm ocean waters into the cavity. Yet, we observe a steep rise in elevation toward the present-day grounding line of Getz at 460 m depth on average, which is a robust feature of the inversion constrained by BedMachine and MBES (Figures 1b–1f). For comparison, the grounding line depths of Pine Island, Thwaites, Kohler, and Smith glaciers are more than 200 m deeper, which promotes higher melt rates and in turn more rapid retreat (Millan et al., 2017; Morlighem et al., 2020; Rignot et al., 2014).

The presence of steep prograde slopes along most of the grounding line should promote greater stability for most of the glaciers that feed GIS, compared with Thwaites, Pine Island, and Smith. In the case of DeVicq Glacier, the grounding line is located on a 700 m deep sill, and only a small portion of the shelf is exposed to warm water (Figure S8). The bed deepens landward into a circular cavity, before rising to a 500 m deep sill, which will probably act as a future stabilizing feature. If DeVicq Glacier is destabilized from this position, however, it could retreat several tens of kilometers along a retrograde slope (Figure S8). The situation is completely different for Berry Glacier to the west. A larger portion of that glacier is exposed to warm water and the 1996–2018 retreat took place over a sector with a steep retrograde slope (Figure 1f). While Berry Glacier may stabilize along a prograde bed in the future, it does not hold a large volume of ice and thus has little potential for sea level rise.

Our bathymetry exhibits a much smoother transition at the front of GIS than the bathymetry of Wei et al. (2020), which is based on a 2D inversion instead of 3D and does not use either BedMachine on land nor MBES at sea as boundary constraints. This independent product exhibits several >300-m abrupt steps in bed topography in numerous places at the ice shelf front, which are significant artifacts limiting its usefulness for modeling ice dynamics and ocean circulation within the cavity. To improve our current product, we would benefit from additional gravity data and direct measurements of seafloor depth, using robotic devices or seismic surveys, especially beneath the main cavity of Getz C. because it is the largest section of GIS without constraints.

Simulated pathways of warm water are significantly different between the three experiments. In Cases I and II, the majority of the heat enters the cavity at the Grant-West opening (Figures 3a and 3b; Table S1, Movie S1) as suggested by the volume transports of the 2007 survey (Table 3 of Jacobs et al., 2013). Most of the ocean heat in Cases I and II thus originates from mCDW having a temperature of ~0.5°C (Figures 3a and 3b). In Case III, the channel between Grant Island and the continent is not resolved (Figure 3c; Movie S1), preventing heat from flowing through the Grant-West opening. The main pathway of heat in Case III thus consists of cross-shelf transport along the western edge of Siple Island (Figure 3c; Table S1, Movie S1). Since this warm water originates directly from the shelf break, it is relatively undiluted and yields warmer temperatures under the ice shelf (~1°C) than in Cases I and II (Figure 3).

Overall, the hydrography for Cases I and II is similar, but for Case III, we find warmer temperatures and a larger discrepancy with observations at the western end of the ice shelf (Figures S3–S6). We conclude that in the case of Getz, the bathymetry plays a critical role in determining heat pathways (Figure 3) and heat transports (Table S1). Indeed, the largest rates of glacier retreat are observed near Berry Glacier, where the sub-ice shelf bathymetry is the deepest and a larger portion of the ice shelf is exposed to warm water, which further supports our analysis. Another major heat pathway in Cases I and II is observed at the Siple-Dean opening (Table S1). The differences in the ice shelf draft between BedMachine and RTopo-2 are relatively small (~45 m, Figure 2e) compared with the differences in bathymetry (Figure 2f) and thus have a smaller impact on the ice shelf melt rates.

Because a deeper bathymetry allows more warm water, and hence higher thermal forcing, to penetrate the cavity, we would expect a higher melt rate with the revised deeper bathymetry, as for Pine Island Bay (Schodlok et al., 2012). Here we find the opposite situation with a total melt water production of 197 Gt/yr in Case I versus 205 Gt/yr in Case III over the same ice shelf area. One factor is that the water temperature at the ice shelf front is substantially warmer in Case III (e.g., western end of Getz) because of cross-shelf transport of relatively undiluted warm water. The friction velocity is another factor influencing basal melt rates in addition to heat transport (Nakayama et al., 2019). These authors find that basal melt rates are more strongly correlated in time with ocean velocities than with water temperature. The ocean model includes these physical processes, but they were not analyzed in detail in this study.

A significant change introduced by the novel bathymetry is a spatial redistribution of the melt rates. The deeper bathymetry allows the model to better capture ocean conditions along the entire grounding line of Getz, especially south of Carney Island (Figures 2a and 2c), where Cases I and II yield more melt near the grounding line, in better agreement with the remote sensing estimates (Figure 2d). Concerning the overestimation of the modeled basal melt rates compared with the remote sensing estimates (Rignot et al., 2013), we noted earlier that water temperatures at the ice shelf front are too high in all study cases, and particularly at the western end of Getz, due to a positive bias in the external ocean thermal forcing to the model (see
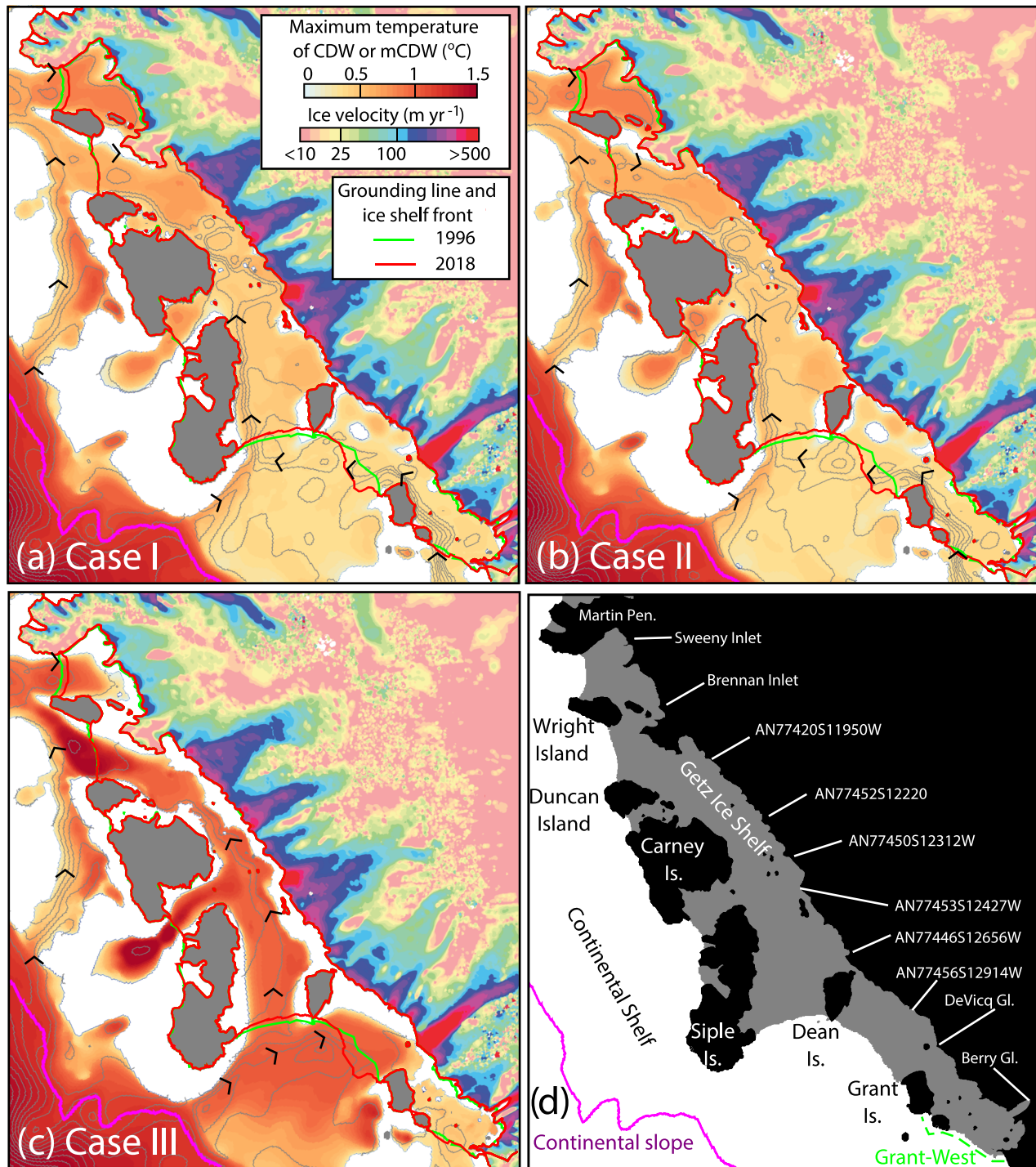
Figure 3. Modeled circulation of warm water on the continental shelf for years 2006–2008. The results shown in the figure are specifically for CDW or mCDW (see the text for the definition of these water masses). Areas where these water masses are absent are represented by solid white. Cases I (a), II (b), and III (c) maximum water temperature within the CDW or mCDW layer (shading, average over years 2006–2008) with streamlines (gray, with direction indicated by the caret symbols; contour interval is 400 m^2/s). Ice velocity data on grounded ice are from Mouginot et al. (2019). The streamlines represent the horizontal circulation at the same depth as the temperature. (d) Map of ice shelf extent (grey), grounded ice (black), and key geographical features mentioned in the text.

Sections 2.2 and 3.2). In addition, differences in observation period, 2003–2008 for Rignot et al. (2013) versus 2006–2008 for the model, may also contribute to this mismatch since water temperatures in the Amundsen Sea increased between 2000 and 2007 (Dutrieux et al., 2014). Despite this melt overestimation, the spatial pattern of ice shelf melt is better reproduced with the new bathymetry, especially near the grounding line. This improvement is significant because an increase in ocean-induced melt near the grounding line has a direct impact on the basal resistance to glacier flow and, in turn, on glacier dynamics (Fürst et al., 2016; Reese et al., 2018; Thomas, 1979).

5. Conclusions

Using a 3D inversion of airborne gravity data collected over GIS, constrained by a bed topography solution from mass conservation inland and seafloor depth data offshore, we provide a comprehensive description of the sub-ice shelf cavity that is smoothly consistent with the boundary conditions and therefore usable in ocean/ice sheet numerical models. We estimate the errors in the bathymetric model to be 50 m, but larger errors are not to be excluded locally in regions with limited in situ observations. We demonstrate the usefulness of the novel bathymetry in an ocean numerical model by obtaining a better spatial agreement with remote sensing estimates in the distribution of melt, especially along the grounding lines. The intensity of melt is overestimated in the model because of anomalously high boundary conditions in water temperature, as reported in previous studies. The ocean model highlights the main pathways of warm water beneath the GIS and, combined with the presence of retrograde bed slopes, explains the rapid, recent evolution of Berry Glacier. The results therefore help in the interpretation of recent glacier evolution in this important sector of West Antarctica.

Data Availability Statement

The data used in the manuscript are archived at datadryad.org (https://doi.org/10.7280/D1XM31). The bathymetry is already part of BedMachine v1 which is publicly available at https://nsidc.org/data/NSIDC-0756/.

References

An, L., Rignot, E., Millan, R., Tinto, K., & Willis, J. (2019). Bathymetry of northwest Greenland using "Ocean Melting Greenland" (OMG) high-resolution airborne gravity and other data. *Remote Sensing*, *11*(2), 131. https://doi.org/10.3390/rs11020131

Arndt, J. E., Schenke, H. W., Jakobsson, M., Nitsche, F. O., Buys, G., Goleby, B., et al. (2013). The International Bathymetric Chart of the Southern Ocean (IBCSO) Version 1.0—A new bathymetric compilation covering circum-Antarctic waters. *Geophysical Research Letters*, *40*, 3111–3117. https://doi.org/10.1002/grl.50413

Assmann, K. M., Darelius, E., Wåhlin, A. K., Kim, T. W., & Lee, S. H. (2019). Warm Circumpolar Deep Water at the western Getz ice shelf front, Antarctica. *Geophysical Research Letters*, *46*, 870–878. https://doi.org/10.1029/2018GL081354

Brisbourne, A. M., Smith, A. M., King, E. C., Nicholls, K. W., Holland, P. R., & Makinson, K. (2014). Seabed topography beneath larsen c ice shelf from seismic soundings. *The Cryosphere*, *8*(1), 1–13. https://doi.org/10.5194/tc-8-1-2014

Cochran, J. R., Jacobs, S. S., Tinto, K. J., & Bell, R. E. (2014). Bathymetric and oceanic controls on Abbot Ice Shelf thickness and stability. *The Cryosphere*, *8*(3), 877–889. https://doi.org/10.5194/tc-8-877-2014

Dinniman, M. S., Klinck, J. M., & Smith, Jr. W. O. (2011). A model study of Circumpolar Deep Water on the west Antarctic Peninsula and Ross Sea continental shelves. *Deep Sea Research Part II*, *58*, 1508–1523. https://doi.org/10.1016/j.dsr2.2010.11.013

Dupont, T. K., & Alley, R. B. (2005). Assessment of the importance of ice-shelf buttressing to ice-sheet flow. *Geophysical Research Letters*, *32*, L04503. https://doi.org/10.1029/2004GL022024

Dutrieux, P., De Rydt, J., Jenkins, A., Holland, P. R., Ha, H. K., Lee, S. H., et al. (2014). Strong sensitivity of Pine Island ice-shelf melting to climatic variability. *Science*, *343*(174), 174–178. https://doi.org/10.1126/science.1244341

Fretwell, P., Pritchard, H. D., Vaughan, D. G., Bamber, J. L., Barrand, N. E., Bell, R., et al. (2013). Bedmap2: Improved ice bed, surface and thickness datasets for Antarctica. *The Cryosphere*, *7*, 375–393. https://doi.org/10.5194/tc-7-375-2013

Fujino, K., Lewis, E. L., & Perkin, R. G. (1974). The freezing point of seawater at pressures up to 100 bars. *Journal of Geophysical Research*, *79*(12), 1792–1797. https://doi.org/10.1029/JC079i012p01792

Fürst, J. J., Durand, G. A., Gillet-Chaulet, F., Tavard, L., Rankl, M., Braun, M., & Gagliardini, O. (2016). The safety band of antarctic ice shelves. *Nature Climate Change*, *6*(5), 479–482. https://doi.org/10.1038/nclimate2912

Gudmundsson, G. H., Paolo, F. S., Adusumilli, S., & Fricker, H. A. (2019). Instantaneous antarctic ice sheet mass loss driven by thinning ice shelves. *Geophysical Research Letters*, *46*, 13,903–13,909. https://doi.org/10.1029/2019GL085027

Haney, R. L. (1991). On the pressure gradient force over steep topography in sigma coordinate models. *Journal of Physical Oceanography*, *21*, 610–619.

Hodgson, D. A., Jordan, T. A., De Rydt, J., Fretwell, P. T., Seddon, S. A., Becker, D., et al. (2019). Past and future dynamics of the Brunt Ice Shelf from seabed bathymetry and ice shelf geometry. *The Cryosphere*, *13*(2), 545–556. https://doi.org/10.5194/tc-13-545-2019

Holland, D. M., & Jenkins, A. (1999). Modeling thermodynamic ice–ocean interactions at the base of an ice shelf. *Journal of Physical Oceanography*, *29*, 1787–1800.

Jacobs, S., Giulivi, C., Dutrieux, P., Rignot, E., Nitsche, F., & Mouginot, J. (2013). Getz ice shelf melting response to changes in ocean forcing. *Journal of Geophysical Research: Oceans*, *118*, 4152–4168. https://doi.org/10.1002/jgrc.20298

Jourdain, N. C., Mathiot, P., Merino, N., Durand, G., Sommer, J. L., Spence, P., et al. (2017). Ocean circulation and sea-ice thinning induced by melting ice shelves in the amundsen sea. *Journal of Geophysical Research: Oceans*, *122*, 2550–2573. https://doi.org/10.1002/2016JC012509

Le Brocq, A. M., Payne, A. J., & Vieli, A. (2010). An improved antarctic dataset for high resolution numerical ice sheet models (albmap v1). *Earth System Science Data*, *2*(2), 247–260. https://doi.org/10.5194/essd-2-247-2010

Maslanyj, M. P. (1987). Seismic bedrock depth measurements and the origin of george vi sound, antarctic peninsula. *British Antarctic Survey Bulletin*, *75*, 51–65.

Mazloff, M. R., Heimbach, P., & Wunsch, C. (2010). An eddy-permitting Southern Ocean state estimate. *Journal of Physical Oceanography*, *40*(5), 880–899. https://doi.org/10.1175/2009jpo4236.1

Millan, R., Rignot, E., Bernier, V., Morlighem, M., & Dutrieux, P. (2017). Bathymetry of the Amundsen Sea Embayment sector of West Antarctica from Operation IceBridge gravity and other data. *Geophysical Research Letters*, *44*, 1360–1368. https://doi.org/10.1002/2016GL072071

Morlighem, M., Rignot, E., Binder, T., Blankenship, D., Drews, R., Eagles, G., et al. (2020). Deep glacial troughs and stabilizing ridges unveiled beneath the margins of the Antarctic ice sheet. *Nature Geoscience*, *13*(2), 132–137. https://doi.org/10.1038/s41561-019-0510-8

Morlighem, M., Rignot, E., Mouginot, J., Seroussi, H., & Larour, E. (2014). Deeply incised submarine glacial valleys beneath the Greenland ice sheet. *Nature Geoscience*, *7*(6), 418–422. https://doi.org/10.1038/ngeo2167

Mouginot, J., Rignot, E., & Scheuchl, B. (2019). Continent-wide, interferometric SAR phase, mapping of Antarctic ice velocity. *Geophysical Research Letters*, *46*, 9710–9718. https://doi.org/10.1029/2019GL083826

Muto, A., Anandakrishnan, S., & Alley, R. B. (2013). Subglacial bathymetry and sediment layer distribution beneath the Pine Island Glacier ice shelf, west Antarctica, modeled using aerogravity and autonomous underwater vehicle data. *Annals of Glaciology*, *54*(64), 27–32. https://doi.org/10.3189/2013AoG64A110

Nakayama, Y., Manucharyan, G., Zhang, H., Dutrieux, P., Torres, H. S., Klein, P., et al. (2019). Pathways of ocean heat towards Pine Island and Thwaites grounding lines. *Scientific Reports*, *9*, 16649. https://doi.org/10.1038/s41598-019-53190-6

Nitsche, F. O., Jacobs, S. S., Larter, R. D., & Gohl, K. (2007). Bathymetry of the Amundsen Sea continental shelf: Implications for geology, oceanography, and glaciology. *Geochemistry, Geophysics and Geosystems*, *8*, Q10009. https://doi.org/10.1029/2007GC001694

Pritchard, H. D., Ligtenberg, S. R., Fricker, H. A., Vaughan, D. G., van den Broeke, M. R., & Padman, L. (2012). Antarctic ice-sheet loss driven by basal melting of ice shelves. *Nature*, *484*, 502–505. https://doi.org/10.1038/nature10968

Reese, R., Gudmundsson, G. H., Levermann, A., & Winkelmann, R. (2018). The far reach of ice-shelf thinning in Antarctica. *Nature Climate Change*, *8*(1), 53–57. https://doi.org/10.1038/s41558-017-0020-x

Rignot, E. (2001). Evidence for rapid retreat and mass loss of Thwaites Glacier, West Antarctica. *Journal of Glaciology*, *47*(157), 213–222.

Rignot, E., Jacobs, S., Mouginot, J., & Scheuchl, B. (2013). Ice-shelf melting around Antarctica. *Science*, *341*, 266–270. https://doi.org/10.1126/science.1235798

Rignot, E., Mouginot, J., Morlighem, M., Seroussi, H., & Scheuchl, B. (2014). Widespread, rapid grounding line retreat of Pine Island, Thwaites, Smith, and Kohler glaciers, West Antarctica, from 1992 to 2011. *Geophysical Research Letters*, *41*, 3502–3509. https://doi.org/10.1002/2014gl060140

Rignot, E., Mouginot, J., Scheuchl, B., van den Broeke, M., van Wessem, M. J., & Morlighem, M. (2019). Four decades of antarctic ice sheet mass balance from 1979–2017. *Proceedings of the National Academy of Sciences*, *116*(4), 1095–1103. https://doi.org/10.1073/pnas.1812883116

Rodriguez, A. R., Mazloff, M. R., & Gille, S. T. (2016). An oceanic heat transport pathway to the Amundsen Sea Embayment. *Journal of Geophysical Research: Oceans*, *121*, 3337–3349. https://doi.org/10.1002/2015JC011402

Schaffer, J., Timmermann, R., Arndt, J. E., Kristensen, S. S., Mayer, C., Morlighem, M., & Steinhage, D.(2016). A global, high-resolution data set of ice sheet topography, cavity geometry and ocean bathymetry. *Earth System Science Data*, *8*, 543–557. https://doi.org/10.5194/essd-8-543-2016

Schodlok, M. P., Menemenlis, D., Rignot, E., & Studinger, M. (2012). Sensitivity of the ice-shelf/ocean system to the sub-ice-shelf cavity shape measured by NASA IceBridge in Pine Island Glacier, west Antarctica. *Annals of Glaciology*, *53*(60), 156–162. https://doi.org/10.3189/2012AoG60A073

Schoof, C. (2007). Ice sheet grounding line dynamics: Steady states, stability, and hysteresis. *Journal of Geophysical Research*, *112*, F03S28. https://doi.org/10.1029/2006JF000664

Shchepetkin, A. F., & McWilliams, J. C. (2003). A method for computing horizontal pressure-gradient force in an oceanic model with a nonaligned vertical coordinate. *Journal of Geophysical Research*, *108*(C3), 3090. https://doi.org/10.1029/2001JC001047

Shchepetkin, A. F., & McWilliams, J. C. (2005). The Regional Oceanic Modeling System (ROMS): A split-explicit, free-surface, topography-following-coordinate oceanic model. *Ocean Modelling*, *9*, 347–404. https://doi.org/10.1016/j.ocemod.2004.08.002

Sherrell, R. M., Lagerstrom, M. E., Forsch, K. O., Stammerjohn, S. E., & Yager, P. L. (2015). Dynamics of dissolved iron and other bioactive trace metals (Mn, Ni, Cu, Zn) in the Amundsen Sea Polynya, Antarctica. *Elementa: Science of the Anthropocene*, *3*(71), 000071. https://doi.org/10.12952/journal.elementa.000071

St-Laurent, P., Yager, P. L., Sherrell, R. M., Stammerjohn, S. E., & Dinniman, M. S. (2017). Pathways and supply of dissolved iron in the Amundsen Sea (Antarctica). *Journal of Geophysical Research: Oceans*, *122*, 7135–7162. https://doi.org/10.1002/2017jc013162

Thomas, R. H. (1979). Ice shelves: A review. *Journal of Glaciology*, *24*(90), 273–286. https://doi.org/10.3189/S0022143000014799

Timmermann, R., Le Brocq, A., Deen, T., Domack, E., Dutrieux, P., Galton-Fenzi, B., et al. (2010). A consistent dataset of Antarctic ice sheet topography, cavity geometry, and global bathymetry. *Earth System Science Data Discuss.*, *2*(2), 261–273. https://doi.org/10.5194/essdd-2-261-2010

Tinto, K. J., & Bell, R. E. (2011). Progressive unpinning of Thwaites Glacier from newly identified offshore ridge: Constraints from aero-gravity. *Geophysical Research Letters*, *38*, L20503. https://doi.org/10.1029/2011GL049026

Tinto, K. J., Padman, L., Siddoway, C. S., Springer, S. R., Fricker, H. A., Das, I., et al. (2019). Ross ice shelf response to climate driven by the tectonic imprint on seafloor bathymetry. *Nature Geoscience*, *12*(6), 441–449. https://doi.org/10.1038/s41561-019-0370-2

Wei, W., Blankenship, D. D., Greenbaum, J. S., Gourmelen, N., Dow, C. F., Richter, T. G., et al. (2020). Getz ice shelf melt enhanced by freshwater discharge from beneath the west antarctic ice sheet. *The Cryosphere*, *14*(4), 1399–1408. https://doi.org/10.5194/tc-14-1399-2020